


Cite this: *RSC Adv.*, 2021, 11, 19630

# Heterostructure $\text{Ni}_3\text{S}_4\text{--MoS}_2$ with interfacial electron redistribution used for enhancing hydrogen evolution†

Jingmin Ge,<sup>a</sup> Jiaying Jin,<sup>a</sup> Yanming Cao,<sup>a</sup> Meihong Jiang,<sup>a</sup> Fazhi Zhang,<sup>a</sup> Hongling Guo<sup>\*b</sup> and Xiaodong Lei<sup>†a</sup>

Developing highly effective and inexpensive electrocatalysts for hydrogen evolution reaction (HER), particularly in a water-alkaline electrolyzer, are crucial to large-scale industrialization. The earth-abundant molybdenum disulfide ( $\text{MoS}_2$ ) is an ideal electrocatalyst in acidic media but suffers from a high overpotential in alkaline solution. Herein, nanospherical heterostructure  $\text{Ni}_3\text{S}_4\text{--MoS}_2$  was obtained via a one-pot synthesis method, in which  $\text{Ni}_3\text{S}_4$  was uniformly integrated with  $\text{MoS}_2$  ultrathin nanosheets. There were abundant heterojunctions in the as-synthesized catalyst, which were verified by X-ray photoelectron spectroscopy (XPS) and high-resolution transmission electron microscopy (HRTEM). The structure features with interfacial electron redistribution was proved by XPS and density functional theory (DFT) calculations, which offered several advantages to promote the HER activity of  $\text{MoS}_2$ , including increased specific surface area, exposed abundant active edge sites and improved electron transfer.  $\text{Ni}_3\text{S}_4\text{--MoS}_2$  exhibited a low overpotential of 116 mV at 10  $\text{mA cm}^{-2}$  in an alkaline solution with a corresponding Tafel slope of 81  $\text{mV dec}^{-1}$  and long-term stability of over 20 h. DFT simulations indicated that the synergistic effects in the system with the chemisorption of H on the (002) plane of  $\text{MoS}_2$  and OH on the (311) plane of  $\text{Ni}_3\text{S}_4$  accelerated the rate-determining water dissociation steps of HER. This study provides a valuable route for the design and synthesis of inexpensive and efficient HER electrocatalyst, heterostructure  $\text{Ni}_3\text{S}_4\text{--MoS}_2$ .

Received 12th April 2021

Accepted 17th May 2021

DOI: 10.1039/d1ra02828f

rsc.li/rsc-advances

## Introduction

With the increasing environmental protection demands, developing sustainable and fossil-free renewable energy plays a major role.<sup>1</sup> Due to its environmentally friendly, zero-emission, high-energy capacity and sustainable merits, hydrogen ( $\text{H}_2$ ) has received extensive attention.<sup>2</sup> The most efficient method to generate  $\text{H}_2$  ( $2\text{H}_2\text{O} \rightarrow 2\text{H}_2 + \text{O}_2$ ) is water splitting by electric power generated from renewable energy sources.<sup>3–5</sup> Currently, some noble metals, such as Pt, Rh and Ir, have been proved to possess excellent catalytic performance as HER electrocatalysts, including low overpotential, low Tafel slope and low impedance.<sup>6,7</sup> However, the exorbitant cost and limited earth abundance of these noble metal materials have hindered their industrialization and commercialization.<sup>8</sup> Therefore, developing electrocatalysts that are low cost, highly

active and stable from nonprecious and earth-abundant metal materials is urgent.

In recent years, earth-abundant 2D  $\text{MoS}_2$  has been considered as an ideal alternative to the precious Pt-based catalysts as the next-generation electrocatalytic material due to its unique structure and chemical properties.<sup>9–11</sup> DFT calculations indicated that  $\text{MoS}_2$  exhibits excellent HER performance in acidic solutions since its edge sites permit a near-optimal hydrogen adsorption free energy ( $\Delta G_{\text{H}^*} = 0.08$  eV).<sup>12</sup> Moreover, the tremendous amount of S sites in the basal plane of pure  $\text{MoS}_2$  are quite inert and not sufficiently utilized.<sup>13</sup> Unfortunately,  $\text{MoS}_2$  has also been found to have poor activity in alkaline media,<sup>14</sup> even though alkaline catalysis is a more widespread application. Numerous strategies have been employed to improve the catalytic activity of 2D  $\text{MoS}_2$ , such as generating the sulfur vacancies,<sup>15</sup> introducing heteroatoms,<sup>16</sup> changing conductive supports.<sup>17</sup> It has been both experimentally and theoretically identified that the fabrication of heterogeneous nanostructures with abundant and accessible exposed active sites is a very effective way for improving the catalytic activity.<sup>18</sup>

$\text{MoS}_2$  decorated with transition metals, such as Fe, Co and Ni, by heterostructure engineering has shown excellent electrocatalytic performance.<sup>19</sup> Because of the versatile electronic structure of these metals and the ability to fill d orbitals with

<sup>a</sup>State Key Laboratory of Chemical Resource Engineering, Beijing University of Chemical Technology, Beijing, 100029, China. E-mail: leixd@mail.buct.edu.cn; Fax: +86-10-64455357

<sup>b</sup>Institute of Forensic Science, Ministry of Public Security, Beijing, 100038, China. E-mail: guohongling1234@163.com

† Electronic supplementary information (ESI) available. See DOI: 10.1039/d1ra02828f



electrons from another transition metal, they provide distinctive catalytic properties. For example, nickel-based catalysts have been shown to have impressive potential for HER electrocatalysts due to their conductivity and low cost.<sup>20,21</sup> Some reports have indicated that constructing heterostructure for MoS<sub>2</sub> *via* introducing nickel sulfides (*e.g.*, Ni<sub>3</sub>S<sub>2</sub>,<sup>22</sup> NiS<sub>2</sub> (ref. 23) and NiS<sup>24</sup>) could provide superior HER activity. However, the intrinsic motivation of the enhanced catalytic performance is not clear. Moreover, the impact of constructing a heterogeneous structure *via* introducing Ni<sub>3</sub>S<sub>4</sub> into MoS<sub>2</sub> on HER performance remains to be studied. Moreover, an in-depth understanding of the interfacial electron redistribution for the improved HER performance is important for its wide application.

In this study, we fabricated the heterostructure Ni<sub>3</sub>S<sub>4</sub>-MoS<sub>2</sub> with a nanospherical morphology *via* a one-step hydrothermal strategy and applied it as an HER catalyst. To improve the electronic conductivity and expose abundant active edge sites of MoS<sub>2</sub>, we constructed the heterostructure *via* introducing Ni<sub>3</sub>S<sub>4</sub> into MoS<sub>2</sub> ultra-thin nanosheets, which significantly enhanced the HER activity. The heterostructure of Ni<sub>3</sub>S<sub>4</sub>-MoS<sub>2</sub> was investigated *via* XPS, SEM and HRTEM techniques. For researching the electron redistribution on the interface of Ni<sub>3</sub>S<sub>4</sub>-MoS<sub>2</sub> and the mechanism of electro-catalysis during HER, we also applied the DFT simulation. It is indicated that the heterostructure Ni<sub>3</sub>S<sub>4</sub>-MoS<sub>2</sub> optimized water dissociation energies and H\* absorption free energy.

## Experimental section

### Materials

Sodium molybdate (vi) dihydrate (Na<sub>2</sub>MoO<sub>4</sub>·2H<sub>2</sub>O), nickel(ii) chloride hexahydrate (NiCl<sub>2</sub>·6H<sub>2</sub>O), urea, sodium sulfide nonahydrate (Na<sub>2</sub>S·9H<sub>2</sub>O) and thiourea (CH<sub>4</sub>N<sub>2</sub>S) were obtained from Beijing Chemical Works. A 5 wt% Nafion solution was obtained from Du Pont China Holding Co., Ltd. A nickel foam (NF) having a thickness of 0.5 mm was bought from Changsha Lyrun New Materials Co., Ltd., and it (cut as 1.0 cm × 1.0 cm in size) was washed with hydrochloric acid, ethanol and deionized water. All other chemicals were of analytical grade and were purchased from Sinopharm Chemical Reagents Co. All chemicals were used without further purification.

### Synthesis of MoS<sub>2</sub>, Ni<sub>3</sub>S<sub>4</sub>-MoS<sub>2</sub> and Ni<sub>4</sub>S<sub>3</sub> nanosheets

3.5 mmol (0.847 g) of Na<sub>2</sub>MoO<sub>4</sub>·2H<sub>2</sub>O and 15 mmol (1.14 g) of thiourea were dissolved in 30 mL of deionized water and dispersed by ultrasonication for 10 min to form a uniform solution. The mixture was transferred into a 50 mL Teflon-lined stainless-steel autoclave and maintained at 180 °C for 24 h. The as-prepared MoS<sub>2</sub> was washed with deionized water and ethanol several times and then dried in a vacuum at 60 °C. Ni<sub>3</sub>S<sub>4</sub>-MoS<sub>2</sub> was synthesized by a simple one-pot step method that was the same as the above process for MoS<sub>2</sub>. However, in the Na<sub>2</sub>MoO<sub>4</sub>·2H<sub>2</sub>O and thiourea mixed solution, different amounts of NiCl<sub>2</sub>·6H<sub>2</sub>O were added. Then, the Ni<sub>3</sub>S<sub>4</sub>-MoS<sub>2</sub> nanosheets were obtained after the same hydrothermal treatment, washing and drying.

Ni<sub>3</sub>S<sub>4</sub> was prepared according to the method in the reported literature.<sup>25</sup> Briefly, 1.5 mmol (0.357 g) of NiCl<sub>2</sub>·6H<sub>2</sub>O and 10 mmol (0.60 g) of urea were dissolved in 30 mL deionized water, and the mixture was dispersed by ultrasonication for 10 min to form a uniform solution. The solution was then transferred into a 50 mL Teflon-lined stainless-steel autoclave and maintained at 130 °C for 2 h. The as-prepared Ni(OH)<sub>2</sub> was washed with deionized water and ethanol several times and then dried in a vacuum at 60 °C. Then, the as-prepared Ni(OH)<sub>2</sub> precursor together with 30 mL of 15 mmol (3.6 g) sodium sulfide (Na<sub>2</sub>S·9H<sub>2</sub>O) aqueous solution was placed in the Teflon-lined stainless-steel autoclave and maintained at 90 °C for 9 h. The as-prepared Ni<sub>3</sub>S<sub>4</sub> was washed with deionized water and ethanol several times and then dried in a vacuum at 60 °C for 12 h.

### Characterization

X-ray diffraction (XRD) patterns were collected on a Rigaku XRD-6000 diffractometer using Cu K $\alpha$  radiation from 3° to 80° at the scan rate of 10° min<sup>-1</sup>. The morphologies were investigated *via* SEM (Zeiss SUPRA 55) at an accelerating voltage of 20 kV. A Brunauer-Emmett-Teller (BET, ASAP 2460) apparatus was used to measure the surface area. HRTEM images were recorded using a JEOL JEM-2010 field-emission transmission electron microscope at an accelerating voltage of 200 kV, combined with energy-dispersive X-ray spectroscopy (EDS). XPS measurements were performed on a Thermo VG ESCALAB 250 X-ray photoelectron spectrometer with Al K $\alpha$  radiation at a pressure of about 2 × 10<sup>-9</sup> Pa. Inductively coupled plasma-optical emission spectrometry (ICP-OES) was adopted to analyze the chemical components of the catalysts.

### Electrochemical measurements

Electrochemical measurements were performed on an electrochemical workstation (CHI 660E, CH Instruments Inc., Chenhua, Shanghai) using a three-electrode mode in an Ar-saturated 1 mol L<sup>-1</sup> KOH aqueous solution. A platinum electrode was used as the counter electrode, a silver/silver chloride (Ag/AgCl) electrode was used as the reference electrode, and the as-fabricated materials were used as the working electrodes. The potentials were converted to the RHE scale using the following Nernst equation:  $E(\text{RHE}) = E(\text{Ag/AgCl}) + 0.059 \text{ pH} + 0.197$ . To accelerate the electrochemical performance tests, 5 mg of the as-prepared catalysts, 2 mg conductive carbon, 35  $\mu\text{L}$  of the 5 wt% Nafion solution and 1 mL anhydrous ethanol were mixed and ultrasonicated for 10 min to form homogeneous catalyst inks. The catalyst inks were dripped respectively onto the as-prepared NF to obtain the working electrodes with a loading of  $\sim 5 \text{ mg cm}^{-2}$ , which were dried at 60 °C for 1 h. The electrochemical impedance spectroscopy (EIS) tests were performed in the frequency range from 100 kHz to 0.1 Hz at an overpotential of 180 mV. The cyclic voltammograms (CV) were obtained between 0.1 and -0.3 V vs. RHE at 100 mV s<sup>-1</sup> to investigate the cycling stability. The long-term stability tests were recorded by taking a chronoamperometric curve current density that reached 10 mA cm<sup>-2</sup>. All data were presented



without IR compensation, and all the electrochemical tests were tested at room temperature.

### Computational methods

All first principles calculations were performed *via* DFT in the Cambridge Sequential Total Energy Package (CASTEP) module in the Materials Studio. The MoS<sub>2</sub> (002) plane consisting of six layers of Mo and S, and the Ni<sub>3</sub>S<sub>4</sub> (311) slab composed of six layers of atoms were constructed as our models, because the (002) plane of MoS<sub>2</sub> and the (311) plane of Ni<sub>3</sub>S<sub>4</sub> were dominant crystal faces from the HRTEM images. The exchange–correlation interactions were treated within the generalized gradient approximation of the Perdew–Burke–Ernzerhof (PBE) type. The plane-wave cutoff energy was 400 eV, and a k-mesh of  $3 \times 3 \times 1$  was adopted to sample the Brillouin zone. The convergence

threshold for energy and Hellmann–Feynman forces on each atom were set to  $10^{-5}$  eV and  $0.01 \text{ eV } \text{\AA}^{-1}$ . Vacuum layers of  $15 \text{ \AA}$  were introduced to minimize interactions between adjacent layers in all supercells.<sup>15</sup> All the atom positions in the model were optimized by the conjugate-gradient optimization procedure.

Gibbs free-energy of the adsorption atomic hydrogen was calculated as the following formula:

$$\Delta G = \Delta E + \Delta ZPE - T\Delta S \quad (1)$$

where  $\Delta E$  is the adsorption energy of adsorbed species on the given unit cell.  $\Delta ZPE$  and  $T\Delta S$  are the zero-point energy and entropy difference of hydrogen in the adsorbed state and the gas phase, respectively. The value of  $ZPE$  and  $TS$  for the

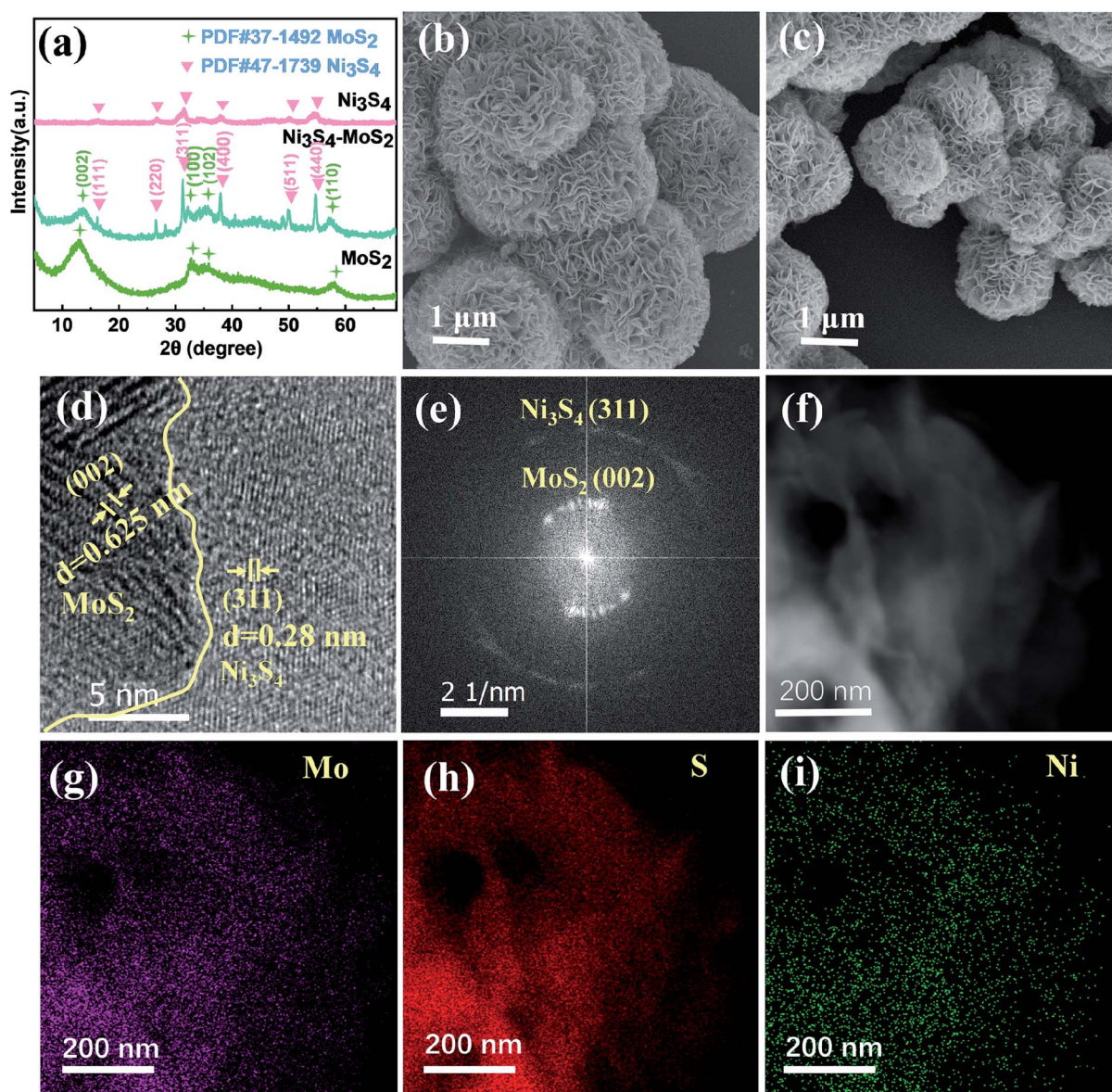


Fig. 1 (a) XRD patterns of Ni<sub>3</sub>S<sub>4</sub>–MoS<sub>2</sub>, Ni<sub>3</sub>S<sub>4</sub> and MoS<sub>2</sub>. (b) SEM image of the Ni<sub>3</sub>S<sub>4</sub>–MoS<sub>2</sub>. (c) SEM image of the MoS<sub>2</sub>. (d) TEM image and (e) corresponding SAED pattern of Ni<sub>3</sub>S<sub>4</sub>–MoS<sub>2</sub>. (f) TEM image of Ni<sub>3</sub>S<sub>4</sub>–MoS<sub>2</sub> and corresponding elemental mappings: Mo (g), S (h) and Ni (i).



adsorbed species were calculated from the vibration frequencies, as shown in the previous literature.<sup>15</sup>

## Results and discussion

### Morphology and structure of Ni<sub>3</sub>S<sub>4</sub>-MoS<sub>2</sub>

A series of Ni<sub>3</sub>S<sub>4</sub>-MoS<sub>2</sub> with different Ni contents were synthesized *via* a one-pot hydrothermal method. The ICP-OES measurements provided the contents of Ni in Ni<sub>3</sub>S<sub>4</sub>-MoS<sub>2</sub>, as shown in Table S1.† The XRD patterns of the Ni<sub>3</sub>S<sub>4</sub>-MoS<sub>2</sub> composite, pure Ni<sub>3</sub>S<sub>4</sub> and MoS<sub>2</sub> are shown in Fig. 1a. For the Ni<sub>3</sub>S<sub>4</sub> and MoS<sub>2</sub> samples, all of their peaks were well matching with the Ni<sub>3</sub>S<sub>4</sub> (JCPDS no. 47-1739) and MoS<sub>2</sub> phases (JCPDS no. 37-1492), respectively. For the XRD pattern of Ni<sub>3</sub>S<sub>4</sub>-MoS<sub>2</sub>, the diffraction peaks at 14.5°, 32.7° and 58.3° corresponded to the (002), (100) and (110) lattice planes of the MoS<sub>2</sub> phase (JCPDS Card no. 37-1492).<sup>26</sup> There are six sharp peaks at 16.2°, 26.6°, 31.3°, 37.9°, 50.0° and 54.7°, which can be indexed to the (111), (220), (311), (400), (511) and (440) planes of Ni<sub>3</sub>S<sub>4</sub> (JCPDS no. 47-1739).<sup>27</sup> The XRD diagram implied the hybrid of these two metal sulfides in Ni<sub>3</sub>S<sub>4</sub>-MoS<sub>2</sub>.

The SEM image of Ni<sub>3</sub>S<sub>4</sub>-MoS<sub>2</sub> identifies that the morphology of the sample is a hierarchical nanosphere composed of nanosheets with a size of about 1 μm and a thickness of about 30 nm (Fig. 1b). By comparison Fig. 1b with c, it is found that the nanosheets of Ni<sub>3</sub>S<sub>4</sub>-MoS<sub>2</sub> are bigger and thinner than that of MoS<sub>2</sub> (average size is about 0.6 μm and thickness is 40 nm, as shown in Fig. S1†). Besides, the heterostructure Ni<sub>3</sub>S<sub>4</sub>-MoS<sub>2</sub> has a larger specific surface area (2.7 m<sup>2</sup> g<sup>-1</sup>) than that of the pure MoS<sub>2</sub> (0.6 m<sup>2</sup> g<sup>-1</sup>). The information illustrates that the construction of the heterojunction increased the surface area of samples. The HRTEM images provide further details of the microstructure for the heterostructure Ni<sub>3</sub>S<sub>4</sub>-MoS<sub>2</sub>. The lattice spacing of 0.625 nm corresponds to the (002) plane of MoS<sub>2</sub>,<sup>28,29</sup> and 0.28 nm corresponds to the (311) plane of Ni<sub>3</sub>S<sub>4</sub>,<sup>30</sup> indicating that the sample consisted of Ni<sub>3</sub>S<sub>4</sub> and MoS<sub>2</sub>. The HRTEM image suggests that the (002) plane of MoS<sub>2</sub> and (311) plane of Ni<sub>3</sub>S<sub>4</sub> constitute important heterointerfaces in the composite (Fig. 1d). The crystal structure of the Ni<sub>3</sub>S<sub>4</sub>-MoS<sub>2</sub> composite was further verified by the select area electron diffraction (SAED) (Fig. 1e). It showed that the inner ring was strong and the outer ring pattern correspond to the (002) plane of the MoS<sub>2</sub> crystal and the (311)

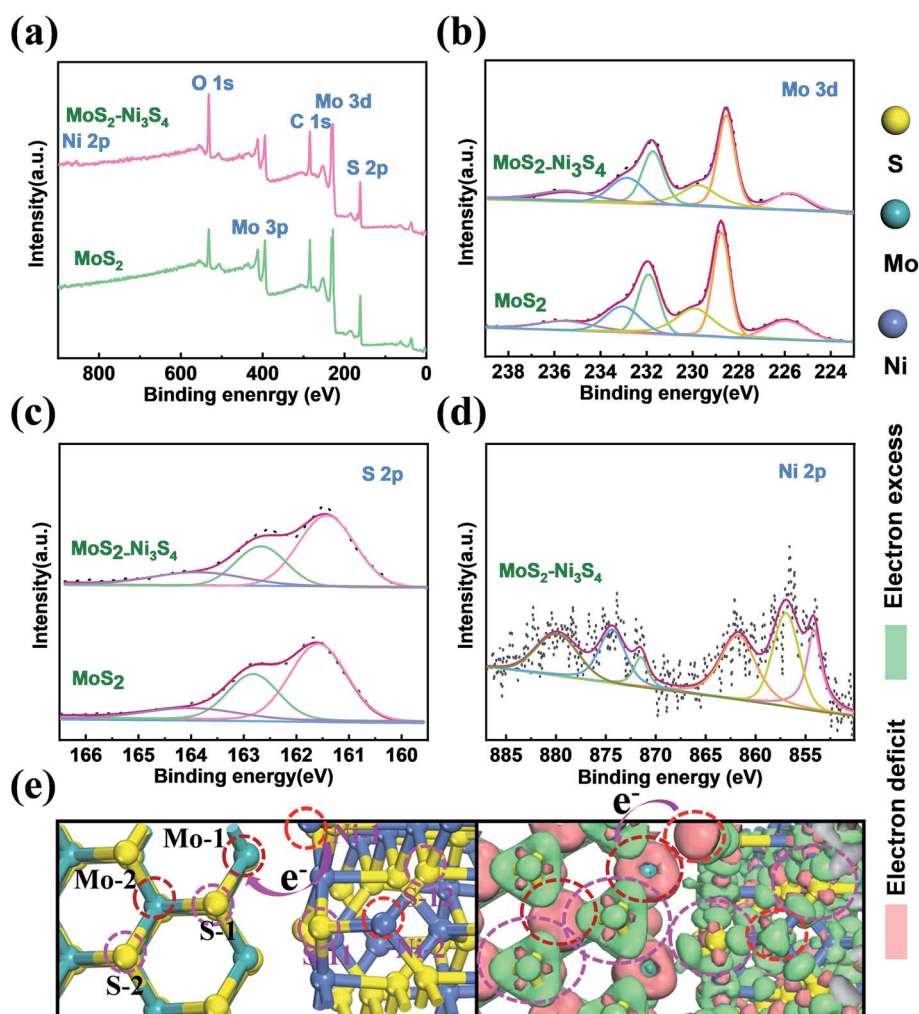


Fig. 2 XPS spectra of Ni<sub>3</sub>S<sub>4</sub>-MoS<sub>2</sub> and MoS<sub>2</sub>: (a) Survey spectra, (b) Mo 3d, (c) S 2p and (d) Ni 2p. (e) Top views of the most stable structure and charge density difference for the Ni<sub>3</sub>S<sub>4</sub>-MoS<sub>2</sub>.



plane of  $\text{Ni}_3\text{S}_4$ , respectively, matching well with the XRD spectra (Fig. 1a). The EDS elemental mapping of  $\text{Ni}_3\text{S}_4\text{-MoS}_2$  indicates that the Mo, S and Ni elements distributed uniformly in the entire nanosheets (Fig. 1f–i), and the contents of Mo, S and Ni of  $\text{Ni}_3\text{S}_4\text{-MoS}_2$  are consistent with the results of ICP-OES tests (Fig. S2 and Table S2†).

XPS spectra were obtained to confirm the chemical composition and valence state of atoms in  $\text{Ni}_3\text{S}_4\text{-MoS}_2$  and pure  $\text{MoS}_2$ , as shown in Fig. 2. It shows the existence of C, Mo, S, Ni and O elements in  $\text{Ni}_3\text{S}_4\text{-MoS}_2$  and the presence of all the elements but no Ni signal in  $\text{MoS}_2$  (Fig. 2a). The O 1s signal was assigned to the absorbed O-containing species, such as  $\text{O}_2$ ,  $\text{CO}_2$  and  $\text{H}_2\text{O}$ . The high-resolution Mo 3d spectra of  $\text{Ni}_3\text{S}_4\text{-MoS}_2$  directly evidence the concurrent presence of  $\text{Mo}^{3+}$  and  $\text{Mo}^{4+}$  (Fig. 2b) with four definite fitting peaks assigned to  $\text{Mo}^{3+}$  ( $3d_{3/2}$  at 231.8 eV and  $3d_{5/2}$  at 228.6 eV) and  $\text{Mo}^{4+}$  ( $3d_{3/2}$  at 232.8 eV and  $3d_{5/2}$  at 229.7 eV), respectively.<sup>17</sup> The binding energies of Mo  $3d_{5/2}$  and Mo  $3d_{3/2}$  in  $\text{Ni}_3\text{S}_4\text{-MoS}_2$  are negative shifts (0.2 eV) compared with the corresponding peaks of pristine  $\text{MoS}_2$ ,<sup>31,32</sup> indicating the lower valence state of Mo in  $\text{Ni}_3\text{S}_4\text{-MoS}_2$ . Thus, the charge transfer behavior from  $\text{Ni}_3\text{S}_4$  to  $\text{MoS}_2$  is determined. The change of Mo valence was ascribed to the electronegativity difference between Mo and Ni, where the introduced  $\text{Ni}_3\text{S}_4$  led to the rearrangement of the electron cloud between Mo and S, thus, forming a new hybridized electronic state. The S 2p spectrum of  $\text{Ni}_3\text{S}_4\text{-MoS}_2$  (Fig. 2c) was deconvoluted into three peaks at 161.4 (S  $2p_{3/2}$ ), 162.6 (S  $2p_{1/2}$ ) and 164.8 eV ( $\text{S}^{2-}$ ),

respectively, and the S 2p shifts to the lower binding energy (about 0.2 eV, S  $2p_{3/2}$  and S  $2p_{1/2}$ ) compared with the pristine  $\text{MoS}_2$  (Fig. 2c), indicating the lower valence state of S in  $\text{Ni}_3\text{S}_4\text{-MoS}_2$ . The result was consistent with the previous reports for other transition metals decorated with  $\text{MoS}_2$ .<sup>33,34</sup> The lower valence state of S in  $\text{Ni}_3\text{S}_4\text{-MoS}_2$  than that in  $\text{MoS}_2$  indicated that S in  $\text{Ni}_3\text{S}_4\text{-MoS}_2$  had a higher electric charge density that was contributed to H adsorption, which helped to improve the HER properties. The Ni 2p spectrum of  $\text{Ni}_3\text{S}_4\text{-MoS}_2$ , as shown in Fig. 2d, exhibits the apparent Ni  $2p_{3/2}$  and  $2p_{1/2}$  peaks at 854.8 and 872.1 eV, respectively, that are attributed to  $\text{Ni}^{2+}$ , and the other peaks at 856.9 and 874.3 eV, attributed to  $\text{Ni}^{3+}$ .<sup>21</sup> Two satellite peaks at 862.1 and 879.6 eV attributed to Ni  $2p_{3/2}$  and  $2p_{1/2}$ , respectively, were observed.<sup>35</sup> It was further confirmed that the material contained compound  $\text{Ni}_3\text{S}_4$ ,<sup>36</sup> which is in agreement with the XRD and HRTEM measurements.

To investigate the electron redistribution on the heterostructure of  $\text{Ni}_3\text{S}_4\text{-MoS}_2$ , the electron density different diagram and the Bader charge analysis was performed by DFT calculations (Fig. 2e and Table S3†). The different electron density diagrams demonstrated that the electric charge densities of Mo and S increased on the interfaces Mo-1, S-1 and S-11 in  $\text{Ni}_3\text{S}_4\text{-MoS}_2$ , compared with that on the base Mo-2, S-2 and S-12 in  $\text{Ni}_3\text{S}_4\text{-MoS}_2$ , indicating that the binding energies of Mo and S in the heterojunction of  $\text{Ni}_3\text{S}_4\text{-MoS}_2$  reduced, which is in accordance with the XPS spectra and Bader charge analysis. The electric charge density of Ni on the interface Ni-1, compared

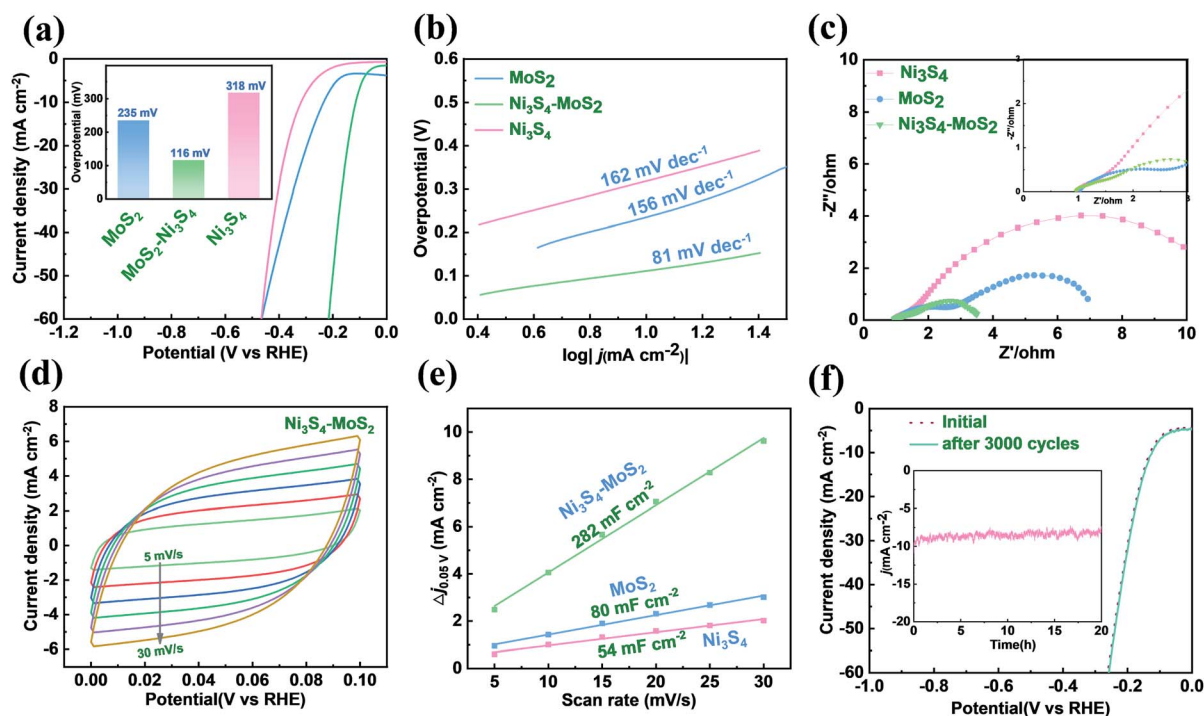


Fig. 3 The HER behavior of  $\text{Ni}_3\text{S}_4\text{-MoS}_2$ ,  $\text{Ni}_3\text{S}_4$  and  $\text{MoS}_2$  in 1 M KOH. (a) The LSV curves and overpotential ( $\eta_{10}$ ) without IR correction. (b) The Tafel slopes. (c) Nyquist plots collected at the overpotential of 180 mV. (d) CV curves of  $\text{Ni}_3\text{S}_4\text{-MoS}_2$  at the scan rates of 5, 10, 15, 20, 25 and 30  $\text{mV s}^{-1}$ , respectively. (e) Differences in current density variation ( $\Delta J = J_a - J_c$ ) at 0.05 V vs. RHE plotted against scan rate fitted to linear regression for estimation of  $C_{dl}$  values of  $\text{Ni}_3\text{S}_4\text{-MoS}_2$ ,  $\text{Ni}_3\text{S}_4$  and  $\text{MoS}_2$ . (f) The initial and 3000th polarization curves of  $\text{Ni}_3\text{S}_4\text{-MoS}_2$ . The inset is the chronoamperometric curve recorded at 10 mA for a continuous 20 h.



with that on the base Ni-2 in  $\text{Ni}_3\text{S}_4\text{-MoS}_2$ , was decreased, indicating that the electrons were transferred from Ni to Mo or S on the interfaces. These data confirmed the electron redistribution in the heterostructure  $\text{Ni}_3\text{S}_4\text{-MoS}_2$ .

### HER catalytic behavior

The HER activities of  $\text{MoS}_2$ ,  $\text{Ni}_3\text{S}_4\text{-MoS}_2$  and  $\text{Ni}_3\text{S}_4$  on NF were measured in a 1 M KOH solution. There was a significant enhancement of the HER activity for  $\text{Ni}_3\text{S}_4\text{-MoS}_2$ , as shown in Fig. 3a. The pure  $\text{MoS}_2$  exhibited an overpotential of 10  $\text{mA cm}^{-2}$  ( $\eta_{10}$ ) at 235 mV, which is in agreement with the reported literature.<sup>37</sup> The  $\eta_{10}$  of  $\text{Ni}_3\text{S}_4\text{-MoS}_2$  is 116 mV, which is much lower than that of the pure  $\text{MoS}_2$  (235 mV) and pristine  $\text{Ni}_3\text{S}_4$  (318 mV). The heterostructure  $\text{Ni}_3\text{S}_4\text{-MoS}_2$  showed superior  $\eta_{10}$  in an alkaline solution and is comparable with the electrocatalysts reported in literature (see Table S4† for more details).<sup>38–40</sup> The HER catalytic performance of the electrocatalysts with different Ni contents in  $\text{Ni}_3\text{S}_4\text{-MoS}_2$  was investigated, as shown in Fig. S3,† indicating that  $\text{Ni}_3\text{S}_4\text{-MoS}_2$  with 7.7 wt% Ni has the lowest overpotential (116 mV) at 10  $\text{mA cm}^{-2}$  in the alkaline solution.

The Tafel curves of  $\text{MoS}_2$ ,  $\text{Ni}_3\text{S}_4\text{-MoS}_2$  and  $\text{Ni}_3\text{S}_4$  on NF are shown in Fig. 3b. The Tafel slope of  $\text{Ni}_3\text{S}_4\text{-MoS}_2$  (81  $\text{mV dec}^{-1}$ ) was much lower than that of  $\text{MoS}_2$  (156  $\text{mV dec}^{-1}$ ), indicating that  $\text{Ni}_3\text{S}_4$  played a key role in promoting the kinetics of HER. The EIS diagrams exhibited similar impedance characteristics, which implied similar electrochemical processes of these samples (Fig. 3c).  $\text{Ni}_3\text{S}_4\text{-MoS}_2$  showed a much lower charge-transfer-resistance ( $R_{\text{ct}}$ ) value when compared with the other catalysts, suggesting that  $\text{Ni}_3\text{S}_4\text{-MoS}_2$  had better charge-transfer property and HER kinetics. In addition, not only the electric conductivity but also the wettability of  $\text{MoS}_2$  was influenced by  $\text{Ni}_3\text{S}_4$ . The contact angle tests of the materials in 1  $\text{mol L}^{-1}$  KOH electrolyte were carried out to explain such influence. The contact angle decreased from 21.36° for  $\text{MoS}_2$  to 15° for  $\text{Ni}_3\text{S}_4\text{-MoS}_2$  (Fig. S3†). It is shown that  $\text{Ni}_3\text{S}_4\text{-MoS}_2$  had better wettability in the KOH electrolyte than that of initial  $\text{MoS}_2$ .

Electrochemical active surface area (ECSA) is a standard parameter applied in the evaluation of electrochemical catalysts. To investigate the exposed active sites, the ECSA of  $\text{Ni}_3\text{S}_4\text{-MoS}_2$ ,  $\text{MoS}_2$  and  $\text{Ni}_3\text{S}_4$  were calculated by the double-layer capacitance ( $C_{\text{dl}}$ ) through plotting CV curves. The CV curves of the samples were tested in the potential range of 0.0–0.1 V at the

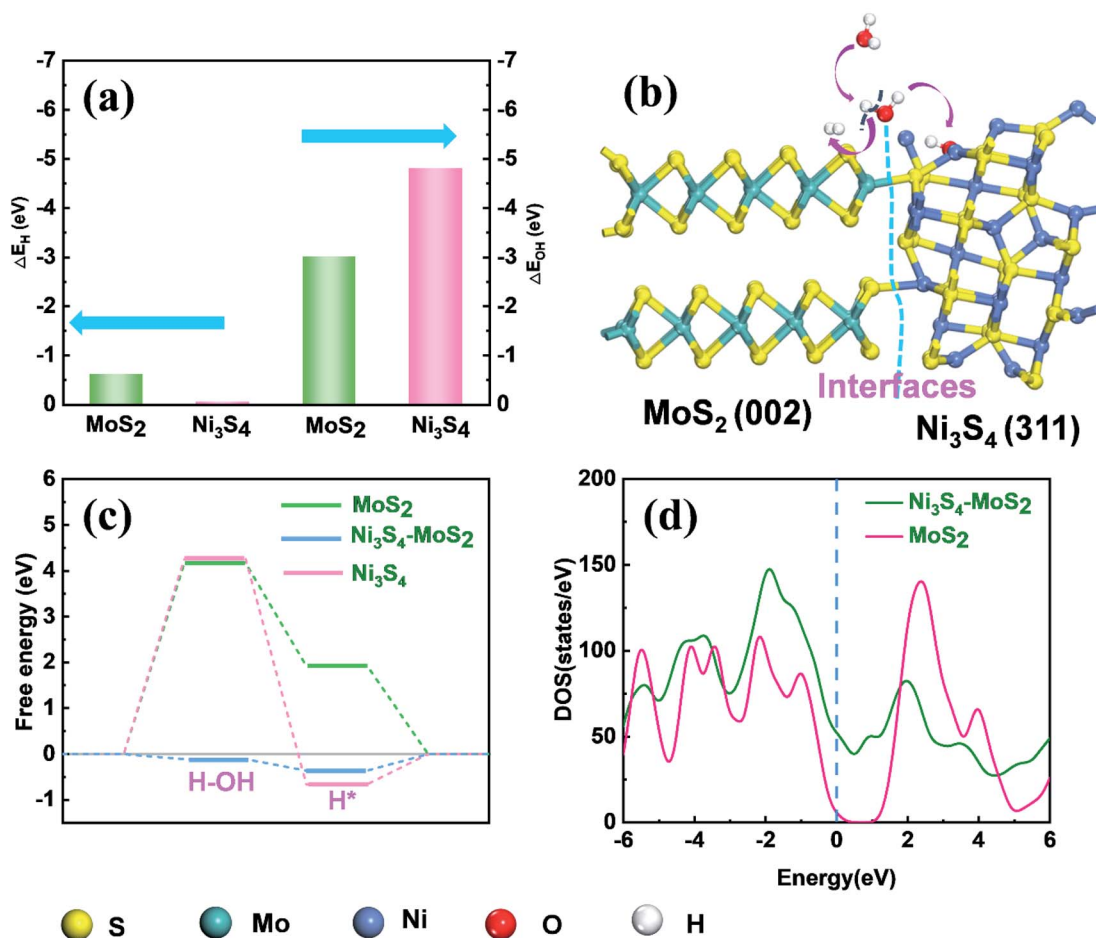


Fig. 4 (a) DFT-calculated adsorption energies of H and OH at different sites on the surfaces of  $\text{Ni}_3\text{S}_4\text{-MoS}_2$ , respectively. (b) The illustration of a mechanism for the electrocatalytic HER under alkaline conditions. (c) Free energy diagrams on the surface of  $\text{MoS}_2$ ,  $\text{Ni}_3\text{S}_4$  and  $\text{Ni}_3\text{S}_4\text{-MoS}_2$  in alkaline solution. (d) DOSs of pristine  $\text{MoS}_2$  and  $\text{Ni}_3\text{S}_4\text{-MoS}_2$ .

scan rates of 5, 10, 15, 20, 25 and 30 mV s<sup>-1</sup> in 1.0 M KOH, respectively (Fig. 3d and S5†). The  $C_{dl}$  value of Ni<sub>3</sub>S<sub>4</sub>-MoS<sub>2</sub> was 282 mF cm<sup>-2</sup>, which is much higher than that of MoS<sub>2</sub> (80 mF cm<sup>-2</sup>) and Ni<sub>3</sub>S<sub>4</sub> (54 mF cm<sup>-2</sup>) (Fig. 3e), indicating that the additional electrochemical active sites were generated after Ni<sub>3</sub>S<sub>4</sub> was introduced. The  $C_{dl}$  value of Ni<sub>3</sub>S<sub>4</sub>-MoS<sub>2</sub> was much more than that of MoS<sub>2</sub> and Ni<sub>3</sub>S<sub>4</sub>, indicating there are more active sites exposed for HER.

To evaluate the long-term stability of the heterostructure Ni<sub>3</sub>S<sub>4</sub>-MoS<sub>2</sub>, it was subjected to 3000 continuous CV cycles in an alkaline environment from 0 to -0.3 V vs. RHE. The LSV curves had no clear changes before and after 3000 CV cycles (Fig. 3f), indicating that Ni<sub>3</sub>S<sub>4</sub>-MoS<sub>2</sub> has excellent catalytic stability during the electrochemical process. Besides, Ni<sub>3</sub>S<sub>4</sub>-MoS<sub>2</sub> has a stable HER current at a constant current of 10 mA *versus* time over a 20 h period in 1 M KOH (Fig. 3f). Simultaneously, the morphology of Ni<sub>3</sub>S<sub>4</sub>-MoS<sub>2</sub> was well preserved (Fig. S6†), demonstrating excellent catalytic stability during the alkaline HER process.

### Mechanism of Ni<sub>3</sub>S<sub>4</sub>-MoS<sub>2</sub> for HER

According to literature,<sup>41,42</sup> DFT calculations were also carried out to gain insight into the underlying mechanism of Ni<sub>3</sub>S<sub>4</sub>-MoS<sub>2</sub> towards the HER activity. In an alkaline medium, the HER reaction mainly includes three steps: water adsorbed on the catalyst, water dissociation, H\* formation and H<sub>2</sub> generation.<sup>43,44</sup> The water dissociation step is considered as the important step for the HER catalytic property in an alkaline solution. The chemisorption free energies of OH ( $\Delta E_{OH}$ ) and H ( $\Delta E_H$ ) on the different sites of Ni<sub>3</sub>S<sub>4</sub>-MoS<sub>2</sub> were calculated, respectively. To study the optimal chemisorption free energies ( $\Delta E$ ), several feasible positions were chosen for the adsorption of OH and H (Fig. S7†). The chemisorption free energy of H adsorbed on the (002) plane of MoS<sub>2</sub> ( $\Delta E_H = -0.81$  eV) was lower than that absorbed on the (311) plane of Ni<sub>3</sub>S<sub>4</sub> ( $\Delta E_H = -0.027$  eV), indicating that H was inclined to be adsorbed on the (002) plane of MoS<sub>2</sub>. Compared with the (002) plane of MoS<sub>2</sub> ( $\Delta E_{OH} = -3.0$  eV), the (311) plane of Ni<sub>3</sub>S<sub>4</sub> showed a predominant binding energy towards OH ( $\Delta E_{OH} = -4.8$  eV), which is attributed to the bonding ability between OH and Ni (Fig. 4a). Therefore, OH is intensely adsorbed on the (311) plane of Ni<sub>3</sub>S<sub>4</sub> and H on the (002) plane of MoS<sub>2</sub>. The appropriate oxidation of Ni in Ni<sub>3</sub>S<sub>4</sub>-MoS<sub>2</sub> contributes to the adsorption energy of OH. Simultaneously, the partial reduction of S in Ni<sub>3</sub>S<sub>4</sub>-MoS<sub>2</sub> is beneficial for the adsorption of H. It demonstrated a synergistic effect of Ni<sub>3</sub>S<sub>4</sub>-MoS<sub>2</sub> with chemisorption of H (on the (002) plane of MoS<sub>2</sub>) and OH (on the (311) plane of Ni<sub>3</sub>S<sub>4</sub>) accelerated the rate-determining water dissociation steps of HER.

The free energy diagrams on the surfaces of MoS<sub>2</sub>, Ni<sub>3</sub>S<sub>4</sub> and Ni<sub>3</sub>S<sub>4</sub>-MoS<sub>2</sub> are shown in Fig. S8.† The  $\Delta G_{H^*}$  of Ni<sub>3</sub>S<sub>4</sub>-MoS<sub>2</sub> was -0.36 eV, which was much lower than that of pure MoS<sub>2</sub> (1.92 eV), indicating the superior capacity of Ni<sub>3</sub>S<sub>4</sub>-MoS<sub>2</sub> for H\* adsorption (Table S4†), which benefited from the electron redistribution between Ni<sub>3</sub>S<sub>4</sub> and MoS<sub>2</sub>. For pure MoS<sub>2</sub>, the free energy barrier of water dissociation  $\Delta G_{H_2O}$  is as high as 4.2 eV, which distinctly hindered the dissociation of H<sub>2</sub>O to H\*.

Moreover, the  $\Delta G_{H_2O}$  of Ni<sub>3</sub>S<sub>4</sub>-MoS<sub>2</sub> was only -0.10 eV, which was much lower than that of MoS<sub>2</sub> (4.2 eV) and Ni<sub>3</sub>S<sub>4</sub> (4.3 eV). It is indicated that the  $\Delta G_{H_2O}$  of Ni<sub>3</sub>S<sub>4</sub>-MoS<sub>2</sub> efficiently decreased because of the existence of a heterostructure. Hence, the HER process on Ni<sub>3</sub>S<sub>4</sub>-MoS<sub>2</sub> is highly accelerated and in accordance with our experimental results.

Moreover, the heterostructure improved the electrical transport efficiency of Ni<sub>3</sub>S<sub>4</sub>-MoS<sub>2</sub>. It is found that the total density of state (DOS) curve of MoS<sub>2</sub> shows a clear band gap at the region around 0 eV, confirming the typical semiconductor characteristic. The peak of the valence band of the heterostructure Ni<sub>3</sub>S<sub>4</sub>-MoS<sub>2</sub> is close to 0 eV (Fig. 4d), leading to the enhanced excitation of charge carriers to the conduction band and showing better electric conductivity, which is consistent with the EIS tests.

## Conclusions

In summary, we fabricated the sphere-shaped heterostructure Ni<sub>3</sub>S<sub>4</sub>-MoS<sub>2</sub> by a one-pot hydrothermal method. The as-synthesized catalyst with the activated interfaces generated abundant active sites and improved the electrical transport efficiency. Benefiting from engineering the heterostructure, the Ni<sub>3</sub>S<sub>4</sub>-MoS<sub>2</sub> demonstrated the low overpotential of 116 mV with the corresponding Tafel slope of 81 mV dec<sup>-1</sup> and long-term stability of over 20 h. DFT calculations proved that the heterostructure Ni<sub>3</sub>S<sub>4</sub>-MoS<sub>2</sub> resulted in electron redistribution, which indicated the presence of a synergistic effect with MoS<sub>2</sub> as the hydrogen acceptor and Ni<sub>3</sub>S<sub>4</sub> as the hydroxyl acceptor, and effectively reduced the intermediate energy barrier of the water dissociation. Hence showing outstanding HER performance in alkaline solution. This work opens the door to develop low-cost and high-activity HER electrocatalyst Ni<sub>3</sub>S<sub>4</sub>-MoS<sub>2</sub> *via* heterostructure engineering.

## Conflicts of interest

The authors declare no competing financial interest.

## Acknowledgements

This work was supported by the National Natural Science Foundation of China (nos 2177060378, 21978023, 21627813 and 21521005), the Program for Changjiang Scholars, Innovative Research Teams in Universities (No. IRT1205), and the Fundamental Research Funds for the Central Universities (No. 12060093063 and XK1803-05).

## References

- 1 Z. W. Seh, J. Kibsgaard, C. F. Dickens, I. Chorkendorff, J. K. Nørskov and T. F. Jaramillo, Combining theory and experiment in electrocatalysis: Insights into materials design, *Science*, 2017, **355**, eaad4998.
- 2 M. S. Dresselhaus and I. L. Thomas, Alternative energy technologies, *Nature*, 2001, **414**, 332–337.



- 3 J. A. Turner, Sustainable hydrogen production, *Science*, 2004, **305**, 972–974.
- 4 V. R. Stamenkovic, D. Strmcnik, P. P. Lopes and N. M. Markovic, Energy and fuels from electrochemical interfaces, *Nat. Mater.*, 2017, **16**, 57–69.
- 5 Y. Zheng, Y. Jiao, A. Vasileff and S.-Z. Qiao, The Hydrogen Evolution Reaction in Alkaline Solution: From Theory, Single Crystal Models, to Practical Electrocatalysts, *Angew. Chem., Int. Ed.*, 2018, **57**, 7568–7579.
- 6 M. Zeng and Y. Li, Recent advances in heterogeneous electrocatalysts for the hydrogen evolution reaction, *J. Mater. Chem. A*, 2015, **3**, 14942–14962.
- 7 Y. Xu and B. Zhang, Recent advances in porous Pt-based nanostructures: synthesis and electrochemical applications, *Chem. Soc. Rev.*, 2014, **43**, 2439–2450.
- 8 H. Zhang, P. An, W. Zhou, B. Y. Guan, P. Zhang, J. Dong and X. W. D. Lou, Dynamic traction of lattice-confined platinum atoms into mesoporous carbon matrix for hydrogen evolution reaction, *Sci. Adv.*, 2018, **4**, eaao6657.
- 9 J. K. Nørskov and C. H. Christensen, Chemistry - Toward efficient hydrogen production at surfaces, *Science*, 2006, **312**, 1322–1323.
- 10 X. Zhang, Z. Lai, C. Tan and H. Zhang, Solution-Processed Two-Dimensional MoS<sub>2</sub> Nanosheets: Preparation, Hybridization, and Applications, *Angew. Chem., Int. Ed.*, 2016, **55**, 8816–8838.
- 11 S. Shi, Z. Sun and Y. H. Hu, Synthesis, stabilization and applications of 2-dimensional 1T metallic MoS<sub>2</sub>, *J. Mater. Chem. A*, 2018, **6**, 23932–23977.
- 12 B. Hinnemann, P. G. Moses, J. Bonde, K. P. Jørgensen, J. H. Nielsen, S. Hørch, I. Chorkendorff and J. K. Nørskov, Biomimetic hydrogen evolution: MoS<sub>2</sub> nanoparticles as catalyst for hydrogen evolution, *J. Am. Chem. Soc.*, 2005, **127**, 5308–5309.
- 13 T. F. Jaramillo, K. P. Jørgensen, J. Bonde, J. H. Nielsen, S. Hørch and I. Chorkendorff, Identification of active edge sites for electrochemical H<sub>2</sub> evolution from MoS<sub>2</sub> nanocatalysts, *Science*, 2007, **317**, 100–102.
- 14 J. Hu, C. Zhang, L. Jiang, H. Lin, Y. An, D. Zhou, M. K. H. Leung and S. Yang, Nanohybridization of MoS<sub>2</sub> with Layered Double Hydroxides Efficiently Synergizes the Hydrogen Evolution in Alkaline Media, *Joule*, 2017, **1**, 383–393.
- 15 J. M. Zhang, X. P. Xu, L. Yang, D. J. Cheng and D. P. Cao, Single-Atom Ru Doping Induced Phase Transition of MoS<sub>2</sub> and S Vacancy for Hydrogen Evolution Reaction, *Small Methods*, 2019, **3**, 1900653.
- 16 Y. Huang, Y. Sun, X. Zheng, T. Aoki, B. Pattengale, J. Huang, X. He, W. Bian, S. Younan, N. Williams, J. Hu, J. Ge, N. Pu, X. Yan, X. Pan, L. Zhang, Y. Wei and J. Gu, Atomically engineering activation sites onto metallic 1T-MoS<sub>2</sub> catalysts for enhanced electrochemical hydrogen evolution, *Nat. Commun.*, 2019, **10**, 982.
- 17 Y. Wang, F. Lu, K. Su, N. Zhang, Y. Zhang, M. Wang and X. Wang, Engineering Mo-O-C interface in MoS<sub>2</sub>@rGO via charge transfer boosts hydrogen evolution, *Chem. Eng. J.*, 2020, **399**, 126018.
- 18 Y. Liu, S. Jiang, S. Li, L. Zhou, Z. Li, J. Li and M. Shao, Interface engineering of (Ni, Fe)S<sub>2</sub>@MoS<sub>2</sub> heterostructures for synergetic electrochemical water splitting, *Appl. Catal., B*, 2019, **247**, 107–114.
- 19 Y. Li, Z. Yin, M. Cui, X. Liu, J. Xiong, S. Chen and T. Ma, Interface engineering of transitional metal sulfide-MoS<sub>2</sub> heterostructure composites as effective electrocatalysts for water-splitting, *J. Mater. Chem. A*, 2021, **9**, 2070–2092.
- 20 M. Gong, D. Y. Wang, C. C. Chen, B. J. Hwang and H. J. Dai, A mini review on nickel-based electrocatalysts for alkaline hydrogen evolution reaction, *Nano Res.*, 2016, **9**, 28–46.
- 21 J. Bao, Y. Zhou, Y. Zhang, X. Sheng, Y. Wang, S. Liang, C. Guo, W. Yang, T. Zhuang and Y. Hu, Engineering water splitting sites in three-dimensional flower-like Co-Ni-P/MoS<sub>2</sub> heterostructural hybrid spheres for accelerating electrocatalytic oxygen and hydrogen evolution, *J. Mater. Chem. A*, 2020, **8**, 22181–22190.
- 22 J. Cao, J. Zhou, Y. Zhang, Y. Wang and X. Liu, Dominating Role of Aligned MoS<sub>2</sub>/Ni<sub>3</sub>S<sub>2</sub> Nanoarrays Supported on Three-Dimensional Ni Foam with Hydrophilic Interface for Highly Enhanced Hydrogen Evolution Reaction, *ACS Appl. Mater. Interfaces*, 2018, **10**, 1752–1760.
- 23 X. Wang, L. Li, Z. Wang, L. Tan, Z. Wu, Z. Liu, S. Gai and P. Yang, NiS<sub>2</sub>/MoS<sub>2</sub> on carbon cloth as a bifunctional electrocatalyst for overall water splitting, *Electrochim. Acta*, 2019, **326**, 134983.
- 24 H. Jiang, K. Zhang, W. Li, Z. Cui, S.-A. He, S. Zhao, J. Li, G. He, P. R. Shearing and D. J. L. Brett, MoS<sub>2</sub>/NiS core-shell structures for improved electrocatalytic process of hydrogen evolution, *J. Power Sources*, 2020, **472**, 228497.
- 25 H. Wang, M. Liang, D. Duan, W. Shi, Y. Song and Z. Sun, Rose-like Ni<sub>3</sub>S<sub>4</sub> as battery-type electrode for hybrid supercapacitor with excellent charge storage performance, *Chem. Eng. J.*, 2018, **350**, 523–533.
- 26 C. Li, M. Liu, H. Ding, L. He, E. Wang, B. Wang, S. Fan and K. Liu, A lightly Fe-doped (NiS<sub>2</sub>/MoS<sub>2</sub>)/carbon nanotube hybrid electrocatalyst film with laser-drilled micropores for stabilized overall water splitting and pH-universal hydrogen evolution reaction, *J. Mater. Chem. A*, 2020, **8**, 17527–17536.
- 27 Y. Zhang, W. Sun, X. Rui, B. Li, H. T. Tan, G. Guo, S. Madhavi, Y. Zong and Q. Yan, One-Pot Synthesis of Tunable Crystalline Ni<sub>3</sub>S<sub>4</sub>@Amorphous MoS<sub>2</sub> Core/Shell Nanospheres for High-Performance Supercapacitors, *Small*, 2015, **11**, 3694–3702.
- 28 J. Deng, H. Li, J. Xiao, Y. Tu, D. Deng, H. Yang, H. Tian, J. Li, P. Ren and X. Bao, Triggering the electrocatalytic hydrogen evolution activity of the inert two-dimensional MoS<sub>2</sub> surface via single-atom metal doping, *Energy Environ. Sci.*, 2015, **8**, 1594–1601.
- 29 H. B. Zhang, L. Yu, T. Chen, W. Zhou and X. W. Lou, Surface Modulation of Hierarchical MoS<sub>2</sub> Nanosheets by Ni Single Atoms for Enhanced Electrocatalytic Hydrogen Evolution, *Adv. Funct. Mater.*, 2018, **28**, 1807086.
- 30 X. Hu, T. Li, Y. Tang, Y. Wang, A. Wang, G. Fu, X. Li and Y. Tang, Hydrogel-Derived Honeycomb Ni<sub>3</sub>S<sub>4</sub>/N, P-C as an





- Efficient Oxygen Evolution Catalyst, *Chem. - Eur. J.*, 2019, **25**, 7561–7568.
- 31 Y. Feng, T. Zhang, J. Zhang, H. Fan, C. He and J. Song, 3D 1T-MoS<sub>2</sub>/CoS<sub>2</sub> Heterostructure via Interface Engineering for Ultrafast Hydrogen Evolution Reaction, *Small*, 2020, **16**, 2002850.
  - 32 S. Qin, T. Yao, X. Guo, Q. Chen, D. Liu, Q. Liu, Y. Li, J. Li and D. He, MoS<sub>2</sub>/Ni<sub>3</sub>S<sub>4</sub> composite nanosheets on interconnected carbon shells as an excellent supercapacitor electrode architecture for long term cycling at high current densities, *Appl. Surf. Sci.*, 2018, **440**, 741–747.
  - 33 Y. Zhao, S. Wei, F. Wang, L. Xu, Y. Liu, J. Lin, K. Pan and H. Pang, Hatted 1T/2H-Phase MoS<sub>2</sub> on Ni<sub>3</sub>S<sub>2</sub> Nanorods for Efficient Overall Water Splitting in Alkaline Media, *Chem. - Eur. J.*, 2020, **26**, 2034–2040.
  - 34 A. Muthurasu, G. P. Ojha, M. Lee and H. Y. Kim, Zeolitic imidazolate framework derived Co<sub>3</sub>S<sub>4</sub> hybridized MoS<sub>2</sub>-Ni<sub>3</sub>S<sub>2</sub> heterointerface for electrochemical overall water splitting reactions, *Electrochim. Acta*, 2020, **334**, 135537.
  - 35 Y. Yang, M.-L. Li, J.-N. Lin, M.-Y. Zou, S.-T. Gu, X.-J. Hong, L.-P. Si and Y.-P. Cai, MOF-derived Ni<sub>3</sub>S<sub>4</sub> Encapsulated in 3D Conductive Network for High-Performance Supercapacitor, *Inorg. Chem.*, 2020, **59**, 2406–2412.
  - 36 K. Wan, J. Luo, C. Zhou, T. Zhang, J. Arbiol, X. Lu, B.-W. Mao, X. Zhang and J. Fransaer, Hierarchical Porous Ni<sub>3</sub>S<sub>4</sub> with Enriched High-Valence Ni Sites as a Robust Electrocatalyst for Efficient Oxygen Evolution Reaction, *Adv. Funct. Mater.*, 2019, **29**, 1900315.
  - 37 J. Kibsgaard, Z. Chen, B. N. Reinecke and T. F. Jaramillo, Engineering the surface structure of MoS<sub>2</sub> to preferentially expose active edge sites for electrocatalysis, *Nat. Mater.*, 2012, **11**, 963–969.
  - 38 X. Hou, A. Mensah, M. Zhao, Y. Cai and Q. Wei, Facile controlled synthesis of monodispersed MoO<sub>3</sub>-MoS<sub>2</sub> hybrid nanospheres for efficient hydrogen evolution reaction, *Appl. Surf. Sci.*, 2020, **529**, 147115.
  - 39 P. Kuang, T. Tong, K. Fan and J. Yu, In Situ Fabrication of Ni-Mo Bimetal Sulfide Hybrid as an Efficient Electrocatalyst for Hydrogen Evolution over a Wide pH Range, *ACS Catal.*, 2017, **7**, 6179–6187.
  - 40 Q. Liu, Z. Xue, B. Jia, Q. Liu, K. Liu, Y. Lin, M. Liu, Y. Li and G. Li, Hierarchical Nanorods of MoS<sub>2</sub>/MoP Heterojunction for Efficient Electrocatalytic Hydrogen Evolution Reaction, *Small*, 2020, **16**, 2002482.
  - 41 F. Lin, Z. Dong, Y. Yao, L. Yang, F. Fang and L. Jiao, Electrocatalytic Hydrogen Evolution of Ultrathin Co-Mo<sub>5</sub>N<sub>6</sub> Heterojunction with Interfacial Electron Redistribution, *Adv. Energy Mater.*, 2020, **10**, 2002176.
  - 42 J. Hu, J. Liu, Z. Chen, X. Ma, Y. Liu, S. Wang, Z. Liu and C. Huang, Insights into the mechanism of the enhanced visible-light photocatalytic activity of a MoS<sub>2</sub>/BiOI heterostructure with interfacial coupling, *Phys. Chem. Chem. Phys.*, 2020, **22**, 22349–22356.
  - 43 C. Hu, L. Zhang and J. Gong, Recent progress made in the mechanism comprehension and design of electrocatalysts for alkaline water splitting, *Energy Environ. Sci.*, 2019, **12**, 2620–2645.
  - 44 C. Zhu, S. Fu, Q. Shi, D. Du and Y. Lin, Single-Atom Electrocatalysts, *Angew. Chem., Int. Ed.*, 2017, **56**, 13944–13960.

